Less density is observed on the cytoplasmic side in comparison to the extracellular side, suggesting that the cytoplasmic loops are less packed than the extracellular loops. The furthest extension of density on the cytoplasmic side is that for helix 6. Evidence to support this comes from site-directed electron paramagnetic resonance (EPR) measurements[17]. Portions of the third cytoplasmic loop have been functionally implicated in interaction with transducin[18], arrestin[19] and rhodopsin kinase[20–22]. However, large segments of the second and third cytoplasmic loops can be deleted without affecting the basic structure of the protein, as reflected by the ability to bind retinal[23].

It is striking that the helix arrangement close to the cytoplasmic surface of rhodopsin is significantly more compact than its extracellular surface (compare sections +12 Å and −8 Å; Fig. 4). This fits well with the stronger conservation of residues in all rhodopsins in this part of the molecule[9]. The area enclosed by the seven helices is 25% smaller in section +12 Å than in section −8 Å. The formation of photoactivated rhodopsin (metarhodopsin II) was shown to be associated with movement of helices[11,12,24]. If this movement expands the cytoplasmic surface area, it would be consistent with the observation that formation of metarhodopsin II occurs with an increase in the overall volume of rhodopsin[25], and provides a newly available binding site for transducin[18].

In conclusion, we have used electron cryo-microscopy to study two-dimensional crystals of frog rhodopsin. Three-dimensional data from tilted specimens have allowed calculation of a three-dimensional map that resolves all seven of the helices, and the approximate tilts of the seven helices have been determined. The molecule can be seen as having a three-layered structure in which helices 2 and 3 keep helices 6 and 7 separated from helix 4. Organized regions of the extracellular surface are seen that include the loop connecting helices 4 and 5 forming the base of the retinal-binding pocket. The cytoplasmic surface is less organized, but there is density for the loop connecting helices 1 and 2, possibly in interaction with the C terminus. The helices are close packed towards the intracellular side, and towards the extracellular side a cavity for retinal binding is formed by helices 3, 4, 5, 6 and 7. □

Methods

Two-dimensional crystals of frog rhodopsin were prepared using Tween 80 extraction of rod cell membranes[7]. The crystal suspension was put on carbon-coated grids, excess buffer was blotted off the specimen, and grids were flash-frozen in liquid ethane. Images of tilted specimens were recorded at liquid nitrogen temperature on a Philips CM12 microscope using a spot-scan procedure and a Gatan cold stage. The tilt angle was restricted to less than 45 deg because with higher tilt angles we were unable to obtain images with enough independent reflections. Amplitudes and phases were extracted as described[6,26] using MRC image-processing software[8]. The overall weighted *R*-factor for agreement between observations and the lattice lines was 36.4% for amplitudes with an overall weighted phase residual of 22.6 deg. A three-dimensional map was calculated after the structure factor amplitudes were scaled using an isotropic temperature factor of $B = -650$ to correct for resolution-dependent fade-out.

Received 4 April; accepted 20 June 1997.

1. Khorana, H. G. Rhodopsin, photoreceptor of the rod cell–an emerging pattern for structure and function. *J. Biol. Chem.* **267,** 1–4 (1992).
2. Baldwin, J. M. Structure and function of receptors coupled to G proteins. *Curr. Opin. Cell Biol.* **6,** 180–190 (1994).
3. Hargrave, P. A. & McDowell, J. H. Rhodopsin and phototransduction–a model system for G-protein-linked receptors. *FASEB J.* **6,** 2323–2331 (1992).
4. Schertler, G. F. X., Villa, C. & Henderson, R. Projection structure of rhodopsin. *Nature* **362,** 770–772 (1993).
5. Baldwin, J. M. The probable arrangement of the helices in G-protein-coupled receptors. *EMBO J.* **12,** 1693–1703 (1993).
6. Unger, V. M. & Schertler, G. F. X. Low resolution structure of bovine rhodopsin determined by electron cryo-microscopy. *Biophys. J.* **68,** 1776–1786 (1995).
7. Schertler, G. F. X. & Hargrave, P. A. Projection structure of frog rhodopsin in two crystal forms. *Proc. Natl Acad. Sci. USA* **92,** 11578–11582 (1995).
8. Crowther, R. A., Henderson, R. & Smith, J. M. MRC image processing programs. *J. Struct. Biol.* **116,** 9–16 (1996).
9. Hargrave, P. A. & McDowell, J. H. Rhodopsin and phototransduction. *Int. Rev. Cytol.* **137B,** 49–97 (1993).
10. Yeagle, P. L., Alderfer, J. L. & Albert, A. D. Structure of the carboxy-terminal domain of bovine rhodopsin. *Nature Struct. Biol.* **2,** 832–834 (1995).
11. Farrens, D. L., Altenbach, C., Yang, K., Hubbell, W. L. & Khorana, H. G. Requirement of rigid-body motion of transmembrane helices for light activation of rhodopsin. *Science* **274,** 768–770 (1996).
12. Sheikh, S. P., Zvyaga, T. A., Lichtarge, O., Sakmar, T. P. & Bourne, H. R. Rhodopsin activation blocked by metal-ion-binding sites linking transmembrane helices C and F. *Nature* **383,** 347–350 (1996).
13. Karnik, S. S. & Khorana, H. G. Assembly of functional rhodopsin requires a disulfide bond between cysteine residues 110 and 187. *J. Biol. Chem.* **265,** 17520–17524 (1990).
14. Han, M. & Smith, S. O. High-resolution structural studies of the retinal–Glu113 interaction in rhodopsin. *Biophys. Chem.* **56,** 23–29 (1995).
15. Zhang, H. Z. *et al.* The location of the chromophore in rhodopsin: a photoaffinity study. *J. Am. Chem. Soc.* **116,** 10165–10173 (1994).
16. Kaushal, S., Ridge, K. D. & Khorana, H. G. Structure and function in rhodopsin – the role of asparagine-linked glycosylation. *Proc. Natl Acad. Sci. USA* **91,** 4024–4028 (1994).
17. Altenbach, C. *et al.* Structural features and light-dependent changes in the cytoplasmic interhelical E-F loop region of rhodopsin: a site-directed spin-labeling study. *Biochemistry* **35,** 12470–12478 (1996).
18. König, B. *et al.* Three cytoplasmic loops of rhodopsin interact with transducin. *Proc. Natl Acad. Sci. USA* **86,** 6878–6882 (1989).
19. Krupnick, J. G., Gurevich, V. V., Schepers, T., Hamm, H. E. & Benovic, J. L. Arrestin–rhodopsin interaction – multi-site binding delineated by peptide inhibition. *J. Biol. Chem.* **269,** 3226–3232 (1994).
20. Wilden, U., Hall, S. W. & Kühn, H. Phosphodiesterase activation by photoexcited rhodopsin is quenched when rhodopsin is phosphorylated and binds the intrinsic 48-kDa protein of rod outer segments. *Proc. Natl Acad. Sci. USA* **83,** 1174–1178 (1986).
21. Palczewski, K., Buczylko, J., Kaplan, M. W., Polans, A. S. & Crabb, J. W. Mechanism of rhodopsin kinase activation. *J. Biol. Chem.* **266,** 12949–12955 (1991).
22. Thurmond, R. L., Creuzet, C., Reeves, P. J. & Khorana, H. G. Structure and function in rhodopsin: peptide sequences in the cytoplasmic loops of rhodopsin are intimately involved in interaction with rhodopsin kinase. *Proc. Natl Acad. Sci. USA* **94,** 1715–1720 (1997).
23. Franke, R. R., Sakmar, T. P., Graham, R. M. & Khorana, H. G. Structure and function in rhodopsin – studies of the interaction between the rhodopsin cytoplasmic domain and transducin. *J. Biol. Chem.* **267,** 14767–14774 (1992).
24. Farahbakhsh, Z. T., Ridge, K. D., Khorana, H. G. & Hubbell, W. L. Mapping light-dependent structural changes in the cytoplasmic loop connecting helices C and D in rhodopsin: a site-directed spin labeling study. *Biochemistry* **34,** 8812–8819 (1995).
25. Lamola, A. A., Yamane, T. & Zipp, A. Effects of detergents and high pressures upon the metarhodopsin\, I ⇔ metarhodopsin\, II equilibrium. *Biochemistry* **13,** 738–745 (1974).
26. Havelka, W. A., Henderson, R. & Oesterhelt, D. Three-dimensional structure of halorhodopsin at 7 Å resolution. *J. Mol. Biol.* **247,** 726–738 (1995).

Acknowledgements. We thank R. Henderson for support and help with image processing; J. H. McDowell for preparing disc membranes; and C. Villa for preparing the rhodopsin model.

Correspondence and requests for materials should be addressed to G.F.X.S. (e-mail: gfx@mrc-lmb.cam.ac.uk).

Surface of bacteriorhodopsin revealed by high-resolution electron crystallography

Yoshiaki Kimura*, Dmitry G. Vassylyev*†, Atsuo Miyazawa*†, Akinori Kidera*†, Masaaki Matsushima‡, Kaoru Mitsuoka§, Kazuyoshi Murata§, Teruhisa Hirai§ & Yoshinori Fujiyoshi§‖

* *Biomolecular Engineering Research Institute (formerly Protein Engineering Institute), 6-2-3 Fureudai, Suita, Osaka 565, Japan*
‡ *Rational Drug Design Laboratory, 4-1-4 Misato, Matsukawa, Fukushima 960-12, Japan*
§ *International Institute for Advanced Research, Matsushita Electric Industrial Co., 3-4 Hikaridai, Seika, Soraku, Kyoto 619-02, Japan*
‖ *Department of Biophysics, Faculty of Science, Kyoto University, Oiwake Kitashirakawa, Sakyou-ku, Kyoto 606-01, Japan*

Bacteriorhodopsin is a transmembrane protein that uses light energy, absorbed by its chromophore retinal, to pump protons from the cytoplasm of bacteria such as *Halobacterium salinarium* into the extracellular space[1,2]. It is made up of seven α-helices, and in the bacterium forms natural, two-dimensional crystals called purple membranes. We have analysed these crystals by electron

† Present addresses: International Institute for Advanced Research (IIAR), Matsushita Electric Industrial Co., Ltd., 3-4 Hikaridai, Seika, Soraku, Kyoto 619-02, Japan (D.G.V.); MRC Laboratory of Molecular Biology, Hills Road, Cambridge CB2 2QH, UK (A.M.); Department of Chemistry, Faculty of Science, Kyoto University, Oiwake Kitashirakawa, Sakyou-ku, Kyoto 606-01, Japan (A.K.).

cryo-microscopy to obtain images of bacteriorhodopsin at 3.0 Å resolution. The structure covers nearly all 248 amino acids, including loops outside the membrane, and reveals the distribution of charged residues on both sides of the membrane surface. In addition, analysis of the electron-potential map produced by this method allows the determination of the charge status of these residues. On the extracellular side, four glutamate residues surround the entrance to the proton channel, whereas on the cytoplasmic side, four aspartic acids occur in a plane at the boundary of the hydrophobic–hydrophilic interface. The negative charges produced by these aspartate residues is encircled by areas of positive charge that may facilitate accumulation and lateral movement of protons on this surface.

Extensive point mutations and biophysical studies of bacteriorhodopsin (relative molecular mass (M_r) 26,548) have revealed crucial amino-acid residues and their roles in the mechanism of the proton pump[3,4], making it the most characterized ion pump. In bacteriorhodopsin, a chromophore, retinal, is attached to Lys 216 by a Schiff base, which is protonated before the retinal absorbs light. When light is absorbed the chromophore is isomerized from all-*trans*- to 13-*cis*-retinal, a change that accompanies the transfer of the Schiff base proton to Asp 85 located nearby on the external side, and the subsequent release of the proton into the external media. The light energy is further used to re-isomerize the chromophore back to all-*trans*-retinal, which accompanies the recovery of the Schiff base proton from Asp 96, which is located to the cytoplasmic side from the Schiff base and is protonated before the absorption of light. Asp 96 subsequently recovers a proton from the cytoplasm, thus completing the photo-reaction cycle. Several other amino-acid side chains are known to affect pumping efficiency.

The spatial arrangement of these residues was proposed previously when a density map from the two-dimensional crystals of bacteriorhodopsin at 3.5 Å resolution was obtained[5]. However, the data were limited owing to the difficulty of obtaining images from the highly tilted (as much as 60 deg) specimen. As the result of this 'missing cone', no interpretable electron-potential density was observed for the loop regions outside the membrane. The work was augmented recently by adding more images to the data and by crystallographic refinement[6]. The results improved the model for the transmembrane portion of the molecule, but the surface structure was still ambiguous, and so the functional role of the surface of bacteriorhodiopsin remained obscure.

We collected structural data from bacteriorhodopsin crystals at 3.0 Å resolution with 90% completeness (Table 1), substantially improving the 'missing cone' problem. An electron cryo-microscope equipped with a stage cooled by liquid helium reduced the rate of radiation damage of the specimens at 4.2 K by as much as 2- and 20-fold compared to the rates at liquid-nitrogen temperature and room temperature, respectively[7]. The electron diffraction patterns were collected to 70 deg tilt at 2.8 Å resolution. The images were collected to 60 deg tilt at 3.0 Å resolution. The phase information from the images was further improved by applying X-ray crystallographic techniques.

In the resulting electron-potential map, almost all of the amino-acid side chains from amino acids 2 to 231, including all loop regions on the surfaces, were clearly observed (Fig. 1b, c). The linking regions between the α-helices exhibited distinct three-dimensional structure as an antiparallel β-sheet, β-turns, and long α-helices protruding from the membrane (Fig. 1a). In the model, the locations of the surface loops were defined by the changes in the distributions of the nitrogen and oxygen atoms of

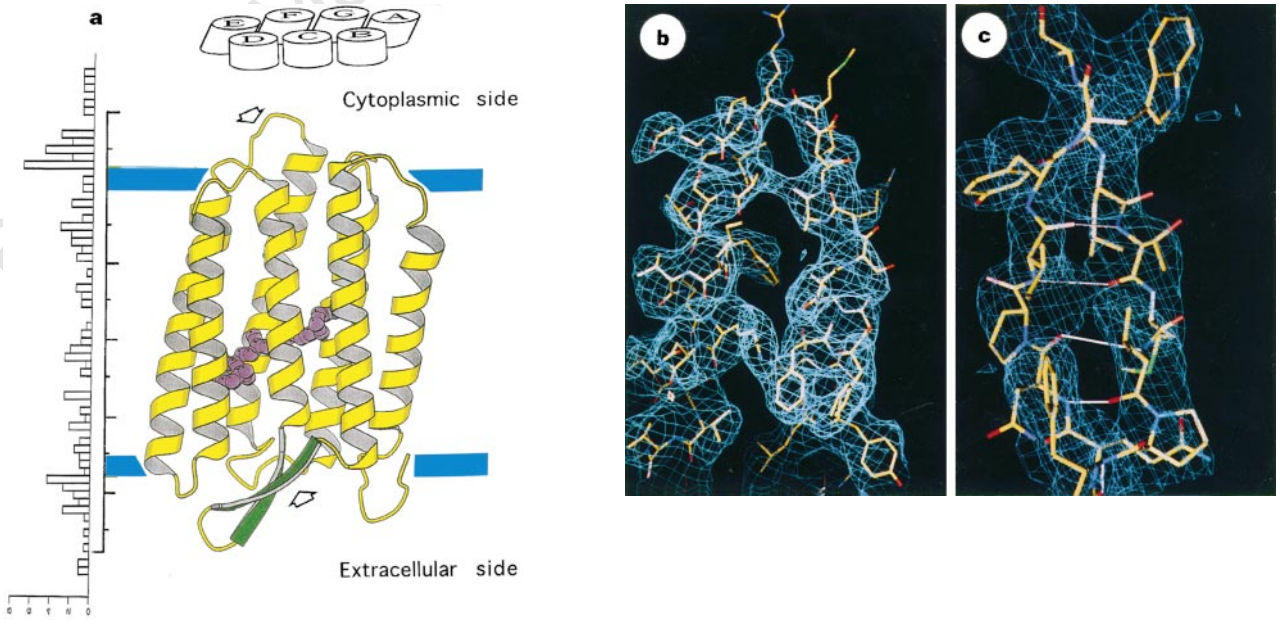

Figure 1 Structure of bacteriorhodopsin. **a**, Ribbon diagram of bacteriorhodopsin and retinal as a ball-and-stick model. The helix assignment is shown above the model. The vertical bar is a 58-Å scale with notches every 5 Å. Blue lines indicate the cytoplasmic and extracellular surfaces, defined as the hydrophobic–hydrophilic interfaces, determined from the distribution of the nitrogen and oxygen atoms in the hydrophilic amino-acid side chains, shown on the left. **b**, The electron-potential map around the loop between the E and F helices (ball-and-stick model), which is extruded from the membrane surface at the cytoplasmic side (upper arrow in **a**). The view is along the membrane. **c**, The electron-potential map around the β-sheet (ball-and-stick model), which links the B and C helices (lower arrow in **a**). Hydrogen bonds within this β-sheet are indicated by solid white lines. These loops are outside membrane surfaces, and were the weakest part for electron crystallography in previous models. The electron-potential densities for all of the other external loops between the internal α-helices were of the same quality.

the hydrophilic amino-acid side chains (Fig. 1a, left), which are likely to reflect the hydrophobic–hydrophilic interfaces of this transmembrane protein. The two peaks in the diagram (Fig. 1a, left) immediately outside the membrane are separated by 41 Å, which agrees well with the cross-sectional view of the membrane observed from the edge[8].

The α-helical transmembrane segments in our model coincide well with the previous model[6], despite some substantial differences in the side-chain conformations. In contrast, the surface structures on both sides of the membrane are very distinct, especially those associated with AB-, BC- and EF-loops (Fig. 1a), which were previously suggested to be disordered[6]; we observed very good

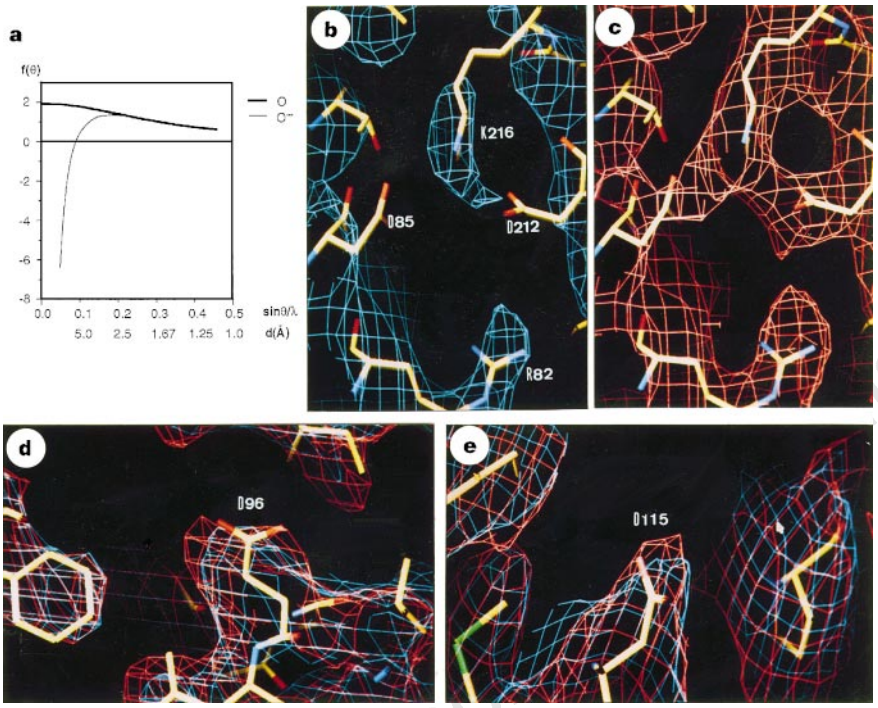

Figure 2 Electron-potential map of the protonated and unprotonated aspartic acids. **a**, Atomic scattering factors of electrons for neutral (thick line) and negatively charged (thin line) oxygen atoms[23]. A negatively charged oxygen exhibits a negative scattering at low resolution. *f*, atomic scattering factor; θ, deflection angle; λ, wavelength of the electron. **b**, Electron-potential densities of bacteriorhodopsin around the retinal Schiff base. The electron-potential map (cyan) was calculated using all data from 54 to 3 Å resolution. **c**, The same view as **b**, but the electron-potential map (orange) was calculated including the structure factors in the resolution range 7 to 3 Å, omitting the low-resolution data, which are strongly affected by the charge effect. **d**, **e**, The electron-potential densities of bacteriorhodopsin around the presumably protonated Asp 96 (**d**) and Asp 115 (**e**). The electron-potential map was calculated either excluding (orange) or including (cyan) the low-resolution reflections.

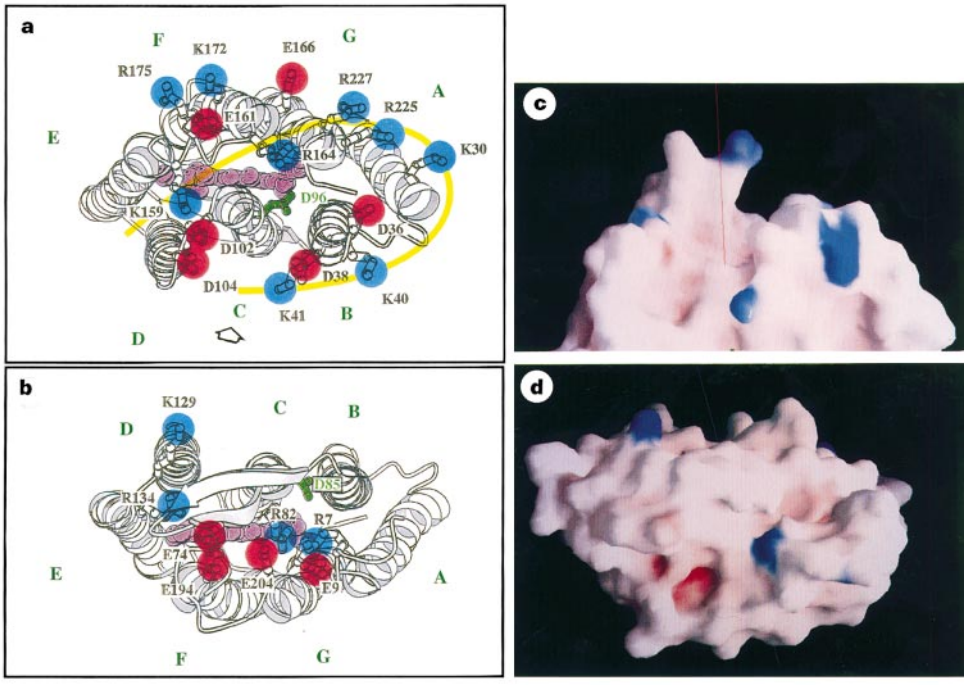

Figure 3 Charge distribution in bacteriorhodopsin. The circles represent negative (red) and positive (blue) charges. Asp 96 and Asp 85 are green to show the donor/acceptor of the proton to/from the Schiff base, which connects retinal and Lys 216. Retinal and Lys 216 are shown in purple. **a**, Charge distribution on the cytoplasmic side of the membrane (input of the proton pump). Asp 96 is surrounded by Asp 36, Asp 38, Asp 102 and Asp 104. This negatively charged cluster is encircled by positively charged protein residues, which are in turn surrounded by negatively charged lipids. **b**, Charge distribution on the extracellular side of the membrane (output of the proton pump). **c**, Solid surface view of the cytoplasmic side of bacteriorhodopsin with a potential calculation (viewed as indicated in **a**). Blue indicates positive and red negative potential. The thin red line is the *z*-axis. The putative proton entrance is in the vicinity of this line. **d**, Solid surface view of the extracellular side of bacteriorhodopsin (corresponding to **b**).

electron-potential densities in these regions (Fig. 1b, c). The orientation of Arg 82 and Asp 96 are now well defined (Fig. 2b, d), whereas the earlier work showed no density[5,6]. The side chain of Arg 82 was protruding toward the Schiff base and formed a charge cluster along with Asp 85, Asp 212 and the Schiff base of retinal Lys 216 (Fig. 2c). The distances between the nearest nitrogen of Arg 82 and the oxygen of Asp 85 or Asp 212 is 6.0 or 5.2 Å, respectively, leaving enough space for water or other molecules among the cluster. All of these residues were known from mutagenesis studies to be essential for the activity of the proton pump[3,4,9–11].

Although most of the protein side chains are represented by good electron-potential densities, a systematic absence of an electron-potential density was observed for several aspartic acids and glutamic acids (Asp 85 and Asp 212 in Fig. 2b). This absence could be explained by the behaviour of the scattering factors of electrons for the negatively charged atoms, as an electron has the same charge (Fig. 2a). When an oxygen is negatively charged, it has a negative scattering factor at low resolution(<11 Å), and so the density in the electron-potential map should be weaker for negatively charged groups. This effect should decrease if the low-resolution data are omitted. We recalculated a map using only the data from 7 to 3 Å. The densities for Asp 85 and Asp 212 were recovered (Fig. 2c), but of course the map became noisier. However, the electron-potential densities of Asp 96 and Asp 115 were only slightly affected by the changes of the resolution limits (Fig. 2d, e). We presume that the observed dependence of the electron-potential density on the resolution limits may provide an insight to the charge status of potentially negatively charged protein residues, as observed effects agree well with results obtained by Fourier transform infrared spectroscopy of the mutant proteins: Asp 85 and Asp 212 are charged, and Asp 96 and Asp 115 are uncharged[11]. If our assumption is correct, then the electron-potential map of bacteriorhodopsin shows that Asp 36, Asp 102 and Glu 194 should be uncharged, whereas other aspartic acid and glutamic acid residues, including Glu 204, should have negative charges, Glu 9 and Glu 166 gave ambiguous results. However, no appreciable effect was observed for the positively charged residues, arginines and lysines, so perhaps the positive-charge effect is less prominent. These conclusions are not definitive, however, because the map with only high-resolution data was noisier.

Among the putatively uncharged residues, Asp 36, Asp 102 and Glu 194 are exposed to water and in theory should be unprotonated. However, Asp 102 is close to Asp 104, which is likely to be charged, and its pK value may be affected by the charge of Asp 104. Furthermore, Asp 36 and Glu 194 are located at the boundary of the hydrophobic–hydrophilic interface. Thus these residues may have a hydrophobic local environment according to the motional freedom that defines the location, as was observed at the boundary of the hydrophobic–hydrophilic interface headgroup regions of the lipid bilayer[12]. The possible low local dielectric constant and its change in the loop region (and in the channel) might have even more significance for the function. The uncharged Asp 115 inside the membrane faces to the lipid area and does not seem to be required for the proton pump to function. The observation of the charged Glu 204 also needs explanation, as it has previously been reported to be protonated[13]. The only direct evidence for its being protonated is the signal of the Fourier transform infrared spectroscopy assigned to Glu 204. It should be noted that the signal was unusually weak and was not changed at alkaline pH, where Glu 204 was supposed to be unprotonated. However, our observation is also not strong enough, as our structure is still noisy and not yet refined. The possibility of estimating charge status provides a significant advantage to electron microscopy relative to X-rays, where atomic

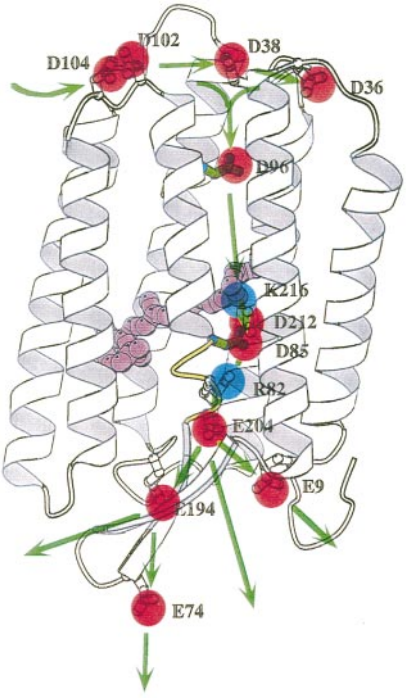

Figure 4 Possible proton pathway in bacteriorhdopsin. The aspartic acids are located in a plane at the hydrophobic–hydrophilic interface on the cytoplasmic side of the membrane. In contrast, the side chains of Glu 204, Glu 194, Glu 74 and Glu 9 on the extracellular side are aligned along the direction perpendicular to the membrane surface. This view corresponds to that of Fig. 1a, except for the part of the ribbon model of C helix, which was replaced with a yellow coil for visualization.

Table 1 Electron crystallographic data

Two-dimensional crystals	
Layer group	*P*3
Lattice constants	$a = b = 62.45$ Å, $c = 100$ Å, $\gamma = 120$ deg
Thickness (Å)	58
Electron diffraction	
No. of diffraction patterns	366
Resolution limit (Å)	2.8
Maximum tilt angle (deg)	70.2
Averaged multiplicity	16.2
Completeness (%)	89
Sampled Fourier space volume ratio within 2.8 Å	95
No. of observed and merged intensities	185,305
No. of independent reflections	9,531
$R_{friedel}$ (%)	10.7
R_{merge} (%)	15.6
Phase observation from images	
No. of observed and used images	129*
Resolution (Å)	3.0
Maximum tilt angle (deg)	61.8
Averaged multiplicity	4.6
Completeness (%)	81
Sampled Fourier space volume ratio within 2.8 Å (%)	87
No. of observed and merged phases	37,218
No. of independent phases	7,129 (1,178 single observations)
Observed phase residuals	26.7†
The final amplitude and phase set	7,842
Resolution (Å)	3.0
Completeness (%)	90

$R_{friedel} = \Sigma_{h,k,Z^*} \left| I_{h,k,Z^*} - I_{-h,-k,-Z^*} \right| / \Sigma_{h,k,Z^*} (I_{h,k,Z^*} + I_{-h,-k,-Z^*})$; $R_{merge} = \Sigma_{h,k,Z^*} \left| I_{h,k,Z^* obs} - I_{h,k,Z^* merged} \right| / \Sigma_{h,k,Z^*} I_{h,k,Z^* merged}$, where I_{h,k,Z^*} and $I_{-h,-k,-Z^*}$ were the intensities of a Friedel-related pair, $I_{h,k,Z^* obs}$ is an observed intensity, and $I_{h,k,Z^* merged}$ is the averaged intensity at the particular h, k, Z^*

* 11 for 0, 20 for 20, 36 for 45 and 62 for 60 deg.

† 16, 21, 26, 32, 38, 44 and 50 deg for 54–7.6, 7.6–5.4, 5.4–4.4, 4.4–3.8, 3.8–3.4, 3.4–3.1 and 3.1–3.0 Å. The f.o.m. angle for 3.3–3.0 Å improved from 60 to 21 deg after phase improvement.

scattering factors are not dependent on the charge. This observation should be confirmed by a refinement of bacteriorhodopsin and by the electron-microscopic studies of other proteins. The effect lies in relatively low resolution, and so electron crystallography of crystals of small molecules with lattice constants less than 11 Å, for instance, could not observe the direct effect of negatively charged oxygen.

Our atomic model reveals the surface details of bacteriorhodopsin, and therefore events at the surface can now be considered in a structural context. Asp 96, which is known to be protonated, acts as a proton donor to the Schiff base[9,10]. There are no dissociable residues near Asp 96, which is within the membrane between the cytoplasmic surface and the retinal Schiff base (green residue in Figs 3a and 4). However, the likely entrance for the protons on the surface is surrounded by negatively charged residues (Asp 36, Asp 38, Asp 102 and Asp 104). Among these, Asp 38 is close to the entrance that leads to Asp 96. All of these negatively charged residues are encircled by positively charged side chains, which are themselves surrounded by lipids with negatively charged headgroups[14]. At the boundary between the protein and the lipids, these positive charges are arranged in a radial manner, but the Asp 102–Asp 104 pair interrupts this positively charged circle. This configuration suggests a likely pathway for proton transfer from the aqueous phase to Asp 96. The protein surface has a large excess of positive charges on the cytoplasmic side. A proton approaching the entrance directly from bulk water would be repelled by the positively charged circle. However, the lipids are negatively charged, and so they may accumulate protons on the surface. The Asp 102–Asp 104 pair is located at the boundary of the positively charged circle and seems to connect the lipid area with the Asp 36–Asp 38–Asp 102 triad within the positively charged circle. This configuration may facilitate lateral proton transfer from the lipid area to the entrance of the bacteriorhodopsin channel. Lateral proton transfer may represent an efficient mechanism of translocating protons from the bulk medium to the entrance of the channel, as the lipid area is much larger than the area of the entrance. The observed uncharged states of Asp 36 and Asp 104 might make this transfer even more efficient by making the proton readily available at the entrance of the proton channel.

The total charge on the extracellular side of the membrane is balanced, with no obvious structural distribution of positive charges. Asp 85 is the proton acceptor from the Schiff base[15]. The naturally deduced proton pathway is from Asp 85 to Glu 204, through Arg 82 or a nearby water molecule. Glu 204 seems to be surrounded by Glu 9, Glu 194 and Glu 74, which are distributed perpendicular to the membrane surface (Fig. 4), in contrast to the planar distribution of aspartates on the cytoplasmic surface of the membrane. This arrangement suggests that the direction of proton transfer on the extracellular side is perpendicular to the membrane surface, rather than lateral to it. Considering the distances between the crucial protein residues, the pathway at the extracellular side of the membrane consists of several routes. The proton can be released by Glu 204, Glu 194, Glu 74 or Glu 9, and so it can be dispersed widely into the surrounding solvent. However, if the indication of the protonation state of Glu 194 is correct, there might be enhanced transfer from either one or all of Glu 204, Glu 194, Glu 74 and Glu 9.

The mechanism of the proton transfer on the cytoplasmic side contrasts strongly with that on the extracellular side: aspartate versus glutamate layout; converging versus diverging pathway; and lateral versus longitudinal transfer, respectively, but both mechanisms have the possibility of multiple pathways. The presence of multiple pathways for proton transfer by bacteriorhodopsin may explain why a single mutation of each particular functional residue does not have a strong influence on the activity of bacteriorhodopsin. As for Asp 102 and Asp 104, single mutations in that pair (D102N or D104N) do not greatly influence proton pump activity[16], but the double mutation (D102N, D104N) considerably reduces the efficiency of the pump[17].

In summary, high-resolution crystallography has allowed us to determine the atomic surface structure of bacteriorhodopsin and to deduce tentatively the charge status of some crucial amino acids, providing an insight into how this seven-α-helix membrane protein works. The disposition of charged residues suggests that the protons diffuse laterally across the membrane surface, increasing the efficiency of the proton translocation from the bulk medium. This may be a general mechanism for many membrane proteins, especially for ion pumps and channels. The divergent mechanism of the proton transfer on the extracellular side of the membrane may also be found in other pumps and channels. □

Methods

Two-dimensional crystals. *Halobacterium salinarium* JW5, a retinal-deficient mutant, was grown as described[18]. All-*trans* retinal was added to the media of the growing culture during log phase in the dark[19]. The purple membrane was purified as described[18]. The membranes were fused as described[20].

Cryo-fixation. Specially ordered surface-polished molybdenum grids were used to minimize the wrinkles induced by cryo-fixation. The grid was covered with a thin carbon film made by slow carbon evaporation onto a freshly cleaved mica surface. The purity of the carbon was greater than 99.9999%; special-grade spectroscopic graphite electrodes were from Hitachi Chemical (Tokyo). The carbon film was floated from the mica to the water surface and was then transferred onto the grid with the water-contacting side on the grid. The purple membrane suspension (2.5 μl) containing 0.4 M citric acid-Na_2HPO_4 buffer, pH 5.5, and 3% trehalose was applied on the carbon film from the grid side. Most of the suspension was drained off with a filter paper for 10–30 s. The grid was then plunged into the liquid ethane, the temperature of which was maintained at 110 K by a Leica (Reichert-Jung) KF80 rapid-freezing apparatus. The differences between our electron-potential map and that described previously[5,6] might be explained by the difference in the specimen conditions; we used trehalose and rapidly froze the specimens, whereas the previous studies[5,6] used completely dried specimens in the presence of glucose. Our specimen, however, is also partly dried; a delay of 10 s before the rapid freezing makes the sample diffract better (better flatness?), but a longer delay makes the diffraction worse. We believe the presence of trehalose prevented the specimen from being dried completely. This partial drying effect was not observed with glucose treatment.

Observation by electron microscopy. The frozen grid was transferred at liquid-nitrogen temperature into the cryo-stage of either a JEOL40000SFX (400 kV) or a JEM3000SFF (300 kV) electron microscope (JEOL, Akishima, Japan)[7], and it was further cooled to 4.2 K. Electron diffraction and images were taken at this temperature with exposures of 15 s and 2 s, respectively, and the total dose on each specimen was kept to less than 10 electrons $Å^{-2}$ by using a low-dose device equipped with the electron microscopes. The images were recorded on Kodak SO-163 film at ×50,000–60,000 magnification, and the electron-diffraction data were recorded with the film or with 1 k × 1 k and 2 k × 2 k slow-scan CCD cameras (Gatan, USA).

Data processing. The initial data processing of the original electron-diffraction patterns and the images was done according to published methods[5,21]. The final data merges were achieved with the CCP4 programs[22]. The crystallographic data are summarized in Table 1).

Electron diffraction. Electron-diffraction patterns were collected between 0 and 70 deg tilt, which covers 95% of the reciprocal space, and the completeness against all the possible diffraction spots was 89% at 2.8 Å (90% at 3.0 Å). Although we estimated the overall resolution limit to be 2.8 Å, the reflections up to 2.2 Å resolution could be collected from specimens with tilt angles less than 20 deg. The highly tilted specimens, however, showed that the reflections perpendicular to the tilt axis tended to be poorer, and so the electron-diffraction patterns were collected with considerable redundancy to ensure multiple observations of as many diffraction spots as possible.

Image. Images were collected from 0 to 60 deg tilt. A plot of the observed amplitudes against the resolution indicated that the good images have similar quality in all directions for all tilt angles. However, the success ratio in obtaining such high-quality data is low for the highly tilted specimens; among the data

summarized in Table 1, all data for untilted specimens, 15 of 20 for 20 deg, 19 of 45 for 45 deg and only 18 of 62 for 60 deg are of high quality. Others were less good but reasonable, with temperature factors in the direction vertical to their tilt axes in the range between 55 and 180 $Å^{-2}$. As a result, the data quality in the direction normal to the tilt axis was poorer at resolutions beyond 4.0 Å, especially in that taken around the 60 deg tilt angle. These phases improved by solvent flattening using the program DM[22] with the molecular envelope determined from the 5-Å resolution initial map, which was obtained accordingly[5]. The calculated phases were combined with the experimental phases. The figures-of-merit (f.o.m.) calculated from the signal-to-noise ratio of the Fourier components in the image processing[5,6] were close to 1.0 and thus too strongly influenced the combination between observed and calculated phases in DM. After several trials in weighting according to resolutions or to the location in reciprocal space, a simple multiplication of all the f.o.m. by 0.8 produced good weightings schema for the phase combination. Further improvement of the signal-to-noise ratio in the map was achieved by averaging the solvent-flattened density and the density calculated from ideal polyalanine α-helices placed to fit in the density. The Ramachandran plot calculated with PROCHECK from the resulting model contains 81% of the residues in the most favourable region; no residues are in the disallowed region of the plot. A simple preliminary positional refinement (fixed *B*-factors) of the current model by XPLOR produced *R*-factor of 24% and free *R*-factor of 37% starting with initial value of 44%. Only the original F_o map calculated with recombined phases and averaged density and the model at the early stage were presented.

Received 21 October 1996; accepted 2 June 1997

1. Oesterhelt, D. & Stoeckenius, W. Rhodopsin-like protein from the purple membrane of *Halobacterium halobium*. *Nature New Biol.* **233,** 149–152 (1971).
2. Oesterhelt, D. & Stoeckenius, W. Functions of a new photoreceptor membrane. *Proc. Natl Acad. Sci. USA* **70,** 2853–2857 (1973).
3. Khorana, H. G. Bacteriorhodopsin, a membrane protein that uses light to translocate protons. *J. Biol. Chem.* **263,** 7439–7442 (1988).
4. Lanyi, J. K. Proton translocation mechanism and energetics in the light-driven pump bacteriorhodopsin. *Biochim. Biophys. Acta* **1183,** 241–261 (1993).
5. Henderson, R. *et al*. A model for the structure of bacteriorhodopsin based on high resolution electron cryo-microscopy. *J. Mol. Biol.* **213,** 899–929 (1990).
6. Grigorieff, N., Ceska, T. A., Downing, K. H., Baldwin, J. M. & Henderson, R. Electron-crystallographic refinement of the structure of bacteriorhodopsin. *J. Mol. Biol.* **259,** 393–421 (1996).
7. Fujiyoshi, Y. *et al*. Development of a superfluid helium stage for high-resolution electron microscopy. *Ultramicroscopy* **38,** 241–251 (1991).
8. Sakata, K., Tahara, Y., Morikawa, K., Fujiyoshi, Y. & Kimura, Y. A method for observing cross-sectional views of biomembranes. *Ultramicroscopy* **45,** 253–261 (1992).
9. Gerwert, K., Hess, B., Soppa, J. & Oesterhelt, D. The role of 96 Asp in proton translocation by bacteriorhodopsin. *Proc. Natl Acad. Sci. USA* **86,** 4943–4947 (1989).
10. Otto, H. *et al*. Aspartic acid-96 is the internal proton donor in the reprotonation of the Schiff base of bacteriorhodopsin. *Proc. Natl Acad. Sci. USA* **86,** 9228–9232 (1989).
11. Braiman, M. S. *et al*. Vibrational spectroscopy of bacteriorhodopsin mutants: light-driven proton transport involves protonation changes of aspartic acid residues 85, 96, and 212. *Biochemistry* **27,** 8516–8520 (1988).
12. Kimura, Y. & Ikegami, A. Local dielectric properties around polar region of lipid bilayer membranes. *J. Membr. Biol.* **85,** 225–231 (1985).
13. Brown, L. S. *et al*. Glutamic acid 204 is the terminal proton release group at the extracellular surface of bacteriorhodopsin. *J. Biol. Chem.* **270,** 27122–27126 (1995).
14. Kushwaha, S. C., Kates, M. & Stoeckenius, W. Comparison of purple membrane from *Halobacterium cutirubrum* and *Halobacterium halobium*. *Biochim. Biophys. Acta* **426,** 703–710 (1976).
15. Subramaniam, S., Greenhalgh, D. A. & Khorana, H. G. Aspartic acid 85 in bacteriorhodopsin functions both as proton acceptor and negative counterion to the Schiff base. *J. Biol. Chem.* **267,** 25730–25733 (1992).
16. Riesle, J., Oesterhelt, D., Dencher, N. A. & Heberle, J. D38 is an essential part of the proton translocation pathway in bacteriorhodopsin. *Biochemistry* **35,** 6635–6643 (1996).
17. Mogi, T., Stern, L. J., Marti, T., Chao, B. H. & Khorana, H. G. Aspartic acid substitutions affect proton translocation by bacteriorhodopsin. *Proc. Natl Acad. Sci. USA* **85,** 4148–4152 (1988).
18. Oesterhelt, D. & Stoeckenius, W. Isolation of the cell membrane of *Halobacterium halobium* and its fractionation into red and purple membrane. *Methods Enzymol.* **31,** 667–678 (1974).
19. Seiff, F., Wallat, I., Ermann, P. & Heyn, M. A neutron diffraction study on the location of the polyene chain of retinal in bacteriorhodopsin. *Proc. Natl Acad. Sci. USA* **82,** 3227–3231 (1985).
20. Baldwin, J. & Henderson, R. Measurement and evaluation of electron diffraction patterns from two-dimensional crystals. *Ultramicroscopy* **14,** 319–333 (1984).
21. Ceska, T. A. & Henderson, R. Analysis of high-resolution electron diffraction patterns from purple membrane labeled with heavy atoms *J. Mol. Biol.* **213,** 539–560 (1990).
22. Collaborate Computational Project No. 4 *Acta Crystallogr. D* **50,** 760–763 (1994).
23. International Union of Crystallography *International table for Crystallography Volume C: Mathematical, Physical and Chemical Tables* (corrected edn) (ed. Wilson, A. J. C.) (Kluwer, Dordrecht, 1995).

Acknowledgements. We thank M. Ikehara for encouragement and support; W. Kühlbrandt and D. N. Wang for help with data processing; R. Henderson, S. Fuller, J. Lanyi, W. Stoeckenius, Y. Harada and J. Sasaki for helpful discussions; T. Miyata for preparing this manuscript; and Digital Equipment Corporation for help with computers.

Correspondence and requests for materials should be addressed to Y.K. (e-mail: kimuray@beri.co.jp). The coordinates of bacteriorhodopsin reported in this paper have been deposited in the Protein Data Bank (Brookhaven), submission no. PDB BNL-6773; id code awaiting assignment.

erratum

Cofilin promotes rapid actin filament turnover *in vivo*

Pekka Lappalainen & David G. Drubin

Nature **388,** 78–82 (1997)

Figure 3a of this Letter was incomplete as published, with two curves being omitted as a result of an error in the reproduction process. The correct figure is shown here.

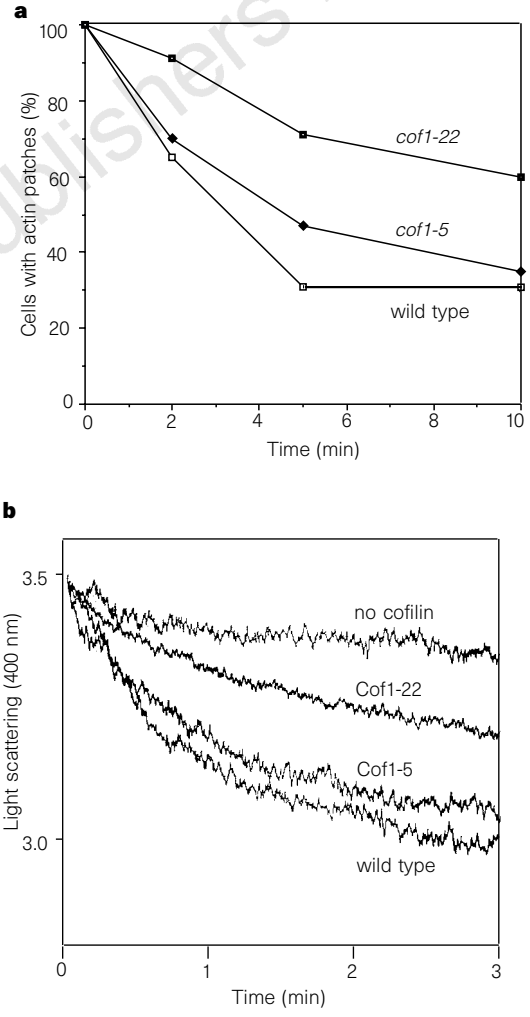

Figure 3 The effects of cofilin mutations on actin-filament depolymerization *in vivo* and *in vitro*. **a**, The percentage of cells with visible actin-filament structures in wild-type, *cof1–5* and *cof1–22* cells at different times after the addition of Lat-A at 25 °C was quantified by rhodamine–phalloidin staining and fluorescent microscopy. For each strain and time point, at least 200 cells from two independent experiments were scored for the presence of actin patches. **b**, The F-actin depolymerization stimulated by recombinant wild-type, *Cof1–5* and *Cof1–22* cofilin was followed by the decrease in light-scattering at 400 nm. Note that dilution of 5 μM yeast actin filaments to 0.5 μM in the absence of cofilin results in slow actin-filament depolymerization. Wild-type cofilin and Cof1–5 cause large increases in the rates of depolymerization, whereas recombinant Cof1–22 causes only a small increase in actin-filament depolymerization rates. The cofilin and yeast actin samples used in these experiments were more than 99% and 95% pure, respectively, based on Coomassie-stained SDS gels (data not shown).